PAPER

A firehose-like aperiodic instability of counter-beaming electron plasmas

IOP Publishing Plasma Physics and Controlled Fusion
Plasma Phys. Control. Fusion **62** (2020) 075006 (8pp) https://doi.org/10.1088/1361-6587/ab8bb5

A firehose-like aperiodic instability of counter-beaming electron plasmas

R A López[1], M Lazar[1,2], S M Shaaban[1,3], S Poedts[1,4] and P S Moya[1,5]

[1] Centre for mathematical Plasma Astrophysics, KU Leuven, Celestijnenlaan 200B, B-3001 Leuven, Belgium
[2] Institut für Theoretische Physik, Lehrstuhl IV: Weltraum- und Astrophysik, Ruhr-Universität Bochum, D-44780 Bochum, Germany
[3] Theoretical Physics Research Group, Physics Department, Faculty of Science, Mansoura University, 35516, Mansoura, Egypt
[4] Institute of Physics, University of Maria Curie-Skłodowska, PL-20-031 Lublin, Poland
[5] Departamento de Física, Facultad de Ciencias, Universidad de Chile, Santiago, Chile

E-mail: rlopez186@gmail.com

Received 31 January 2020, revised 17 April 2020
Accepted for publication 21 April 2020
Published 29 May 2020

Abstract

Depending on the physical conditions involved, beam plasma systems may reveal new unstable regimes triggered by wave instabilities of different natures. We show through linear theory and numerical simulations the existence of an aperiodic electromagnetic instability which solely develops and controls the stability of two symmetric plasma populations counter-moving along the regular magnetic field with a relative drift, v_d, small enough to not exceed the particle thermal speed, α_e. Emerging at highly oblique angles this mode resembles properties of the aperiodic firehose instability driven by temperature anisotropy. The high growth rates achieved with increasing the relative drift or/and decreasing the plasma beta parameter lead to significant saturation levels of the fluctuating magnetic field power, which explain the relatively fast relaxation of electrons. For $v_d > \alpha_e$ this instability can coexist with the electrostatic two-stream instability, dominating the long-term dynamics of the plasma as soon as v_d has relaxed to values smaller than the thermal speed.

Supplementary material for this article is available online

Keywords: particle-in-cell simulations, firehose instability, two-stream instability

(Some figures may appear in colour only in the online journal)

1. Introduction

Whether magnetized or not, plasma systems are highly susceptible to aperiodic instabilities of electromagnetic fields [1–5]. These are zero-frequency ($\omega = 0$) waves with spatial propagation, i.e. with finite wave-numbers ($k \neq 0$), but locally their amplitude is purely growing in time with a rate ($\gamma > 0$), usually much higher than that of the periodic modes. Notorious in unmagnetized plasmas are the so-called Weibel or magnetic instabilities, which can be induced by the kinetic anisotropies of plasma populations, e.g. temperature anisotropy or counter-beaming populations [6, 7], and are frequently invoked to explain the origin of cosmological magnetic field seeds, e.g. in the early Universe [8, 9], and the filamentation of energetic plasma beams [5, 10, 11]. However, the influence of a guiding stationary magnetic field on filamentation instability is not clear yet, Vlasov and particle-in-cell (PIC) simulations showing contradictory results [5, 10]. Instead, the aperiodic mirror [2, 12, 13] and firehose instabilities [1, 14, 15] may develop efficiently in finite beta plasmas, constraining any anisotropic temperature [13, 16, 17] induced by magnetic compression or adiabatic expansion along the magnetic field lines (e.g. solar outflows in the heliosphere).

Counter-beaming plasma systems are of particular interest in astrophysical and experimental setups [18–21], i.e. in fusion and plasma experiments, where the interest is to avoid the formation of escaping beams and stabilize plasma systems,

while in astrophysics, plasma beams are widely invoked, likely, at the origin of various emissions and fluctuations which trigger their relaxation [22–24]. Energetic beams with speed exceeding the mean thermal speed are highly susceptible to electrostatic instabilities [25] and the electromagnetic modes may only hardly compete in nonrelativistic conditions [9]. Less energetic beams with drifting (or beaming) speed lower than thermal speed have not been explored in detail in the past. Such beams guided by the magnetic fields lines can be associated with the incipient beaming formation in plasmas [26–28]. In this case the electrostatic instability may not develop, but an extended analysis of the full wave-vector spectrum of instabilities unveil electromagnetic growing modes expected to destabilize the more or less symmetric plasma beams [24]. Better known are probably the regimes of asymmetric beams, such as the electron strahls observed in the solar wind, less dense but hotter than core electrons. These strahls are responsible for the main electron heat flux, and can be destabilized either by the whistler heat-flux instability, highly conditioned by their thermal asymmetry, or by the firehose heat flux instability, if the beaming speed exceeds the thermal speed of the strahl [29–32]. In the latter case, the interplay (or competition) with the electrostatic instabilities predicted by linear theory must also be investigated.

In the present paper, using linear theory and PIC simulations, we show that in a magnetized plasma the field-aligned counter-beaming populations of electrons can excite an aperiodic instability with linear properties similar to the aperiodic electron firehose instability (AEFHI) driven by anisotropic temperatures $T_{\parallel} > T_{\perp}$, where $\parallel$ and $\perp$ denote directions with respect to the magnetic field. A parallel can be made with the Weibel and filamentation instabilities [6, 7] in unmagnetized plasmas, one driven by temperature anisotropies (Weibel) and the other one induced by counter-beaming plasmas, but both triggered by the same mechanism and both showing similar properties. In order to demonstrate the same similarity between firehose-like instabilities, here we assume symmetric counter-beams, i.e. with the same densities, temperatures and counter-beaming speeds, and isolate from electrostatic competitors (e.g. the electrostatic two-stream instability) by considering beaming speeds less than thermal speeds. However, for a complete parametrization certain limit conditions are also described, allowing us to understand how this instability may convert, e.g. for less symmetric or more energetic beams, and connect to other instability conditions already described in the literature. The results are discussed in the next section, starting with an extended linear analysis of the instability growth rates and their variations with the angle of propagation and the main plasma parameters. The analysis is completed with insights from PIC simulations, which allow us to understand the long term evolution of growing fluctuations and their back reaction on particles, contributing to the relaxation of counter-beams. Possible interplay of the aperiodic beaming firehose instability with the electrostatic two-stream instability (ETSI) is also discussed. In the last section we summarize our main results and present conclusions.

2. Results

2.1. Linear theory

We consider an electron-proton plasma, with the electrons represented by two counter-beaming populations (in a frame fixed to protons). The electron velocity distribution function (VDF) is written as

$$f_e\left(v_\perp, v_\parallel\right) = \frac{n_1}{n_0} f_1\left(v_\perp, v_\parallel\right) + \frac{n_2}{n_0} f_2\left(v_\perp, v_\parallel\right), \qquad (1)$$

where n_0 is the total electron number density (equal to the proton density $n_0 = n_p$), n_j is the number density, and f_j the velocity distribution function, of the jth beam. Each individual beam distribution function is an isotropic drifting Maxwellian of the form

$$f_j(v_\perp, v_\parallel) = \frac{1}{\pi^{3/2}\alpha_j^3} \exp\left\{-\frac{v_\perp^2}{\alpha_j^2} - \frac{(v_\parallel - U_j)^2}{\alpha_j^2}\right\}, \qquad (2)$$

where $\alpha_j = (2k_B T_j/m_e)^{1/2}$ is the thermal velocity and U_j the drift velocity of the jth beam. Using the zero current condition, the drift velocities are related by $U_2 = -n_1/n_2\, U_1$. On the other hand, protons are described by an isotropic non-drifting Maxwellian VDF, with the same temperature as electrons.

We start the present analysis by assuming two symmetric counter-beaming electron populations, with $n_1 = n_2 = 0.5n_0$, $|U_1| = |U_2| = v_d$, and $\alpha_1 = \alpha_2 = \alpha_e$. The plasma beta parameter and plasma frequency are calculated with the total electron density, i..e., $\beta_j = 8\pi n_0 k_B T_j/B_0^2$, $\omega_{pe} = (4\pi n_0 k_B T/m_e)^{1/2}$, and for the plasma to gyro-frequency ratio we consider $\omega_{pe}/\Omega_e = 20$. For a fixed value of the electron plasma beta, β_e, we analyze the full spectrum of unstable modes triggered by the relative drift of electron populations. To do so, using the dispersion solver developed in reference [4, 33], we derive the unstable solutions for arbitrary angle of propagation.

Figure 1 displays the growth rate, γ/Ω_e, obtained for $\beta_e = 2.0$ and various drift velocities, increasing from left to right, $v_d/c = 0.045$, 0.05, 0.06, and 0.065, as a function of the angle of propagation, θ, and normalized wave number, ck/ω_{pe}, where c is the speed of light. Here we have used the same color bar for all cases. In each panel, the fastest growing mode corresponding to the maximum growth-rate is marked with a white asterisk. Starting from the left, for $v_d/c = 0.045$, the fastest growing mode is located at $ck/\omega_{pe} \approx 0.48$ and $\theta \approx 52^\circ$, with a relatively small maximum growth rate $\gamma_{\max}/\Omega_e \approx 0.034$. This is an oblique and purely aperiodic unstable mode, with zero real frequency, $\omega_r = 0$ (not shown here). The other cases clearly show that this unstable mode is markedly stimulated by the increase of drift velocity. In the second panel, for $v_d/c = 0.05$, the fastest growing mode develops with a higher growth rate $\gamma_{\max}/\Omega_e \approx 0.08$ for a wave number $ck/\omega_{pe} \approx 0.56$, and more oblique angle $\theta \approx 59.4^\circ$. For $v_d = 0.06$ in the third panel peaking growth rate is even higher, $\gamma_{\max}/\Omega_e \approx 0.19$, located at $\theta \approx 66.6^\circ$ and $ck/\omega_{pe} \approx 0.68$. In the last panel, for higher drifts $v_d/c = 0.065$ the theory also predicts the ETSI, that can be observed for high wave numbers (around $ck/\omega_{pe} \approx 1.0$) and

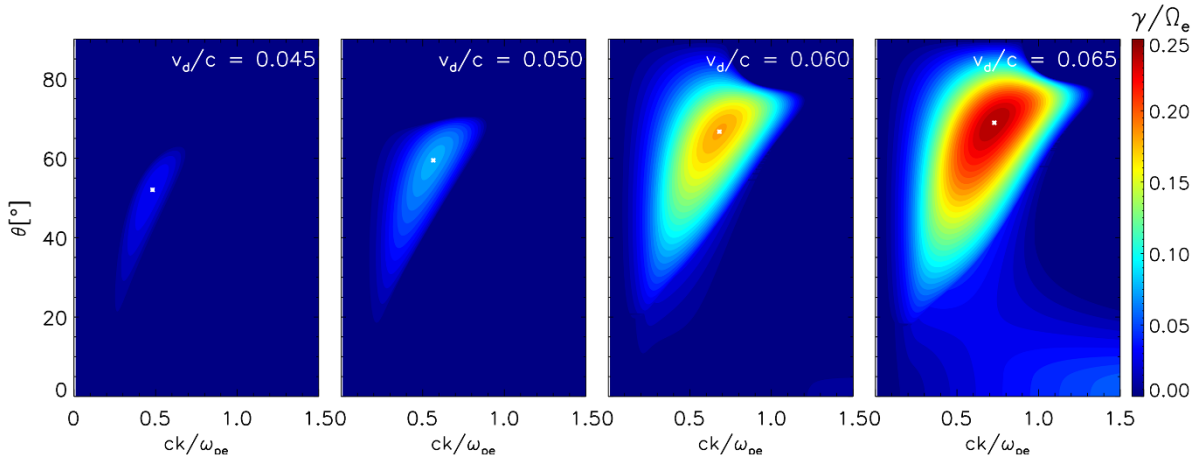

Figure 1. Linear growth rates for BEFHI, γ/Ω_e, for $\beta_e = 2$ and various drift velocities, $v_d/c = 0.045$, 0.05, 0.06, and 0.065.

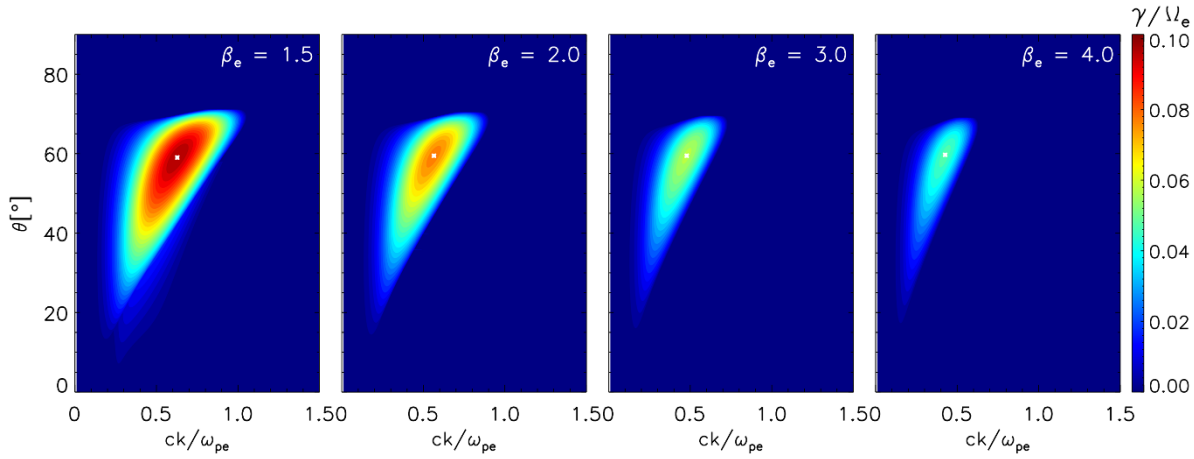

Figure 2. Linear growth rates for BEFHI, γ/Ω_e, for $v_d/c = 0.05$ and various electron plasma beta, $\beta_e = 1.5$, 2.0, 3.0, and 4.0.

small (parallel and quasi-parallel) angles of propagation, but with very low growth rates, $\gamma/\Omega_e < 0.1$. For this case the fastest growing mode is also given by the oblique instability, with $\gamma_{\max}/\Omega_e \approx 0.25$ located at $\theta \approx 68.9^\circ$ and $ck/\omega_{pe} \approx 0.72$. Qualitatively and also quantitatively, this aperiodic instability is very similar to the AEFHI driven by electron temperature anisotropy $A = T_\perp/T_\parallel < 1$, see figure 5 in reference [15] and confirmations from simulations in reference [4]. Indeed, both of these unstable modes develop in the same range of unstable wave numbers and the same interval of propagation angles, and both are triggered by an excess of kinetic (free) energy of electrons in direction parallel to the background magnetic field. Moreover, maximum growth rates may reach comparable values for reasonable temperature anisotropy, e.g. $A_e = 0.2$ for AEFHI and $v_d/c = 0.065$ for our beaming instability. It is for these reasons that from now on we will name this instability as the beaming electron firehose-like instability (BEFHI).

In figure 2 we show the influence of plasma beta parameter on BEFHI. Growth rates are derived as functions of θ and kc/ω_{pe} for a fixed $v_d/c = 0.05$ but different $\beta_e = 1.5$, 2.0, 3.0 and 4.0. The maximum growth rate decreases, respectively, as (from left to right) $\gamma_{\max}/\Omega_e \approx 0.1$, 0.08, 0.059, and 0.049, making clear that this instability is inhibited by increasing β_e. The angle of propagation of the fastest growing mode is not much affected by the increase of plasma beta, remaining around $\theta \approx 59^\circ$ for all cases. However, the wave number of the fastest growing mode decreases as β_e increases, $ck/\omega_{pe} \approx 0.62$, 0.56, 0.47, and 0.42, from left to right, respectively.

The results of our linear analysis can be summarized with plots, as in figure 3. Shown with a color palette in logarithm scale, maximum growth rates of BEFHI (including those from figures 1 and 2) are derived in terms of electron plasma beta (β_e) and drift velocity (v_d/c). With black contour lines we have highlighted the lowest values $\gamma_{\max}/\Omega_e = 0.01$, 0.03, 0.06, 0.1 and 0.15, usually taken as thresholds approaching marginal stability ($\gamma_{\max} \to 0$). The (aperiodic) ETSI becomes dominant for drift velocities higher than thermal velocity, above the white line marking $v_d = \alpha_e$, with growth rates higher, and much higher than BEFHI. Thus, depending on the plasma parameters the ETSI and BEFHI are expected to coexist and compete.

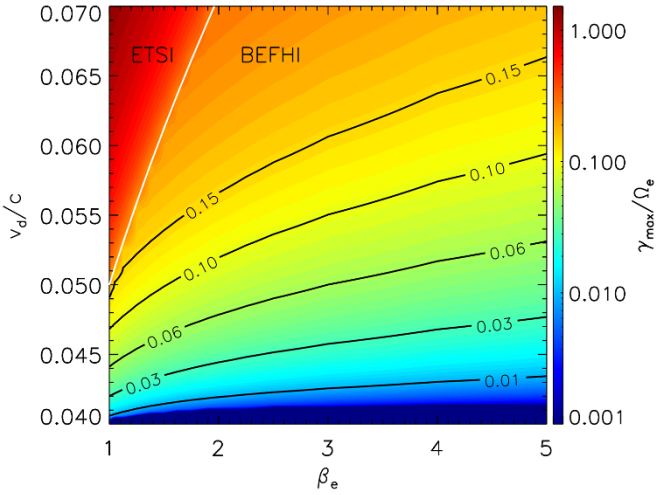

Figure 3. Maximum growth rate as a function of plasma beta and drift velocity, β and v_d/c. The color palette is in logarithm scale. In white we show the contour for $v_d = \alpha_e$.

Table 1. Initial plasma parameters for the simulation.

Parameter	Case I	Case II	Case III
β_e	4.0	2.0	1.0
v_d/c	0.07	0.06	0.06
v_d/α_e	0.70	0.85	1.20
$\gamma_{\max}/\Omega_e$	0.21	0.19	1.91

2.2. PIC simulations

In order to study the evolution of BEFHI and its competition with quasi-parallel modes, we ran a series of 2.5D PIC simulation, adapted from the KEMPO1 explicit code of Matsumoto and Omura [34]. We use a spatial grid of $n_x \times n_y = 1024 \times 1024$, with 400 particles per species per grid cell. The box length is $L_x = L_y = 307.2\, c/\omega_{pe}$, with the cell width $\Delta x = \Delta y = 0.3\, c/\omega_{pe}$. We use a realistic mass ratio $m_p/m_e = 1836$, and the same plasma to gyro-frequency ratio $\omega_{pe}/\Omega_e = 20$. The background magnetic field is in the x-axis direction, $\mathbf{B}_0 = B_0\,\hat{\mathbf{x}}$. Finally, the time step is $\Delta t = 0.01/\omega_{pe}$, and the simulation runs until $t_{\max} = 81.92/\Omega_e$. To save computational resources we have run cases with large growth rates, such that, the instabilities can develop in a shorter temporal window. The three cases selected are listed in table 1.

We first study two cases for low drifts $v_d < \alpha_e$, when the BEFHI is dominant but behaves markedly different: Case I for $v_d/c = 0.07$ ($v_d/\alpha_e = 0.7$) and $\beta = 4$, with the fastest growing mode corresponding to $\gamma_{\max}/\Omega_e \approx 0.21$; and Case II for $v_d/c = 0.06$ ($v_d/\alpha_e = 0.85$) and $\beta = 2$, with the fastest growing mode of $\gamma_{\max}/\Omega_e \approx 0.19$. The initial electron (total) velocity distributions, as used in the simulations for each of these two cases, are shown in figure 4. Predictions from linear theory for these two cases are shown in figure 5, left panels. For a comparison with the results from simulations (right panels) here the growth rates are plotted in k_x–k_y plane, top panel for Case I and bottom panel for Case II. Right panels in figure 5

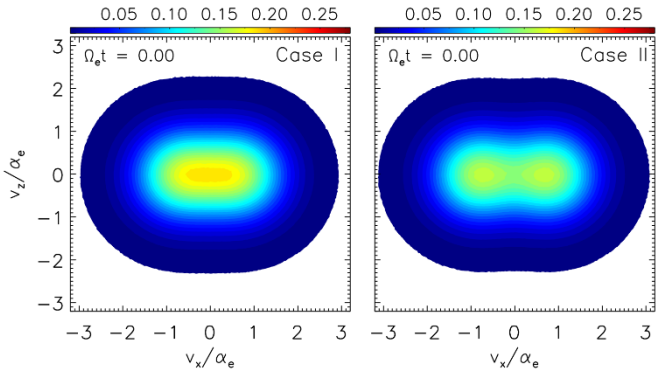

Figure 4. Initial electron velocity distribution function, $f(v_x, v_y)$, in the v_x–v_z space, for both cases.

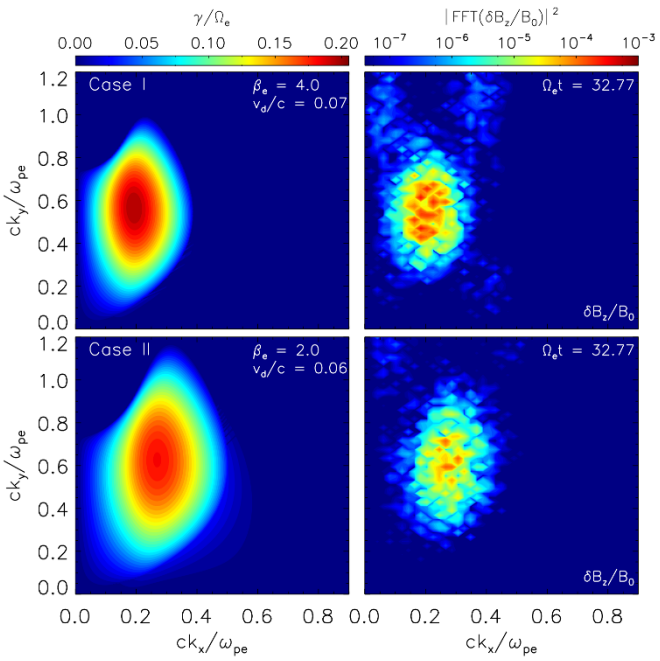

Figure 5. Left panels: growth rates from linear theory. Right panel: Power spectra of the transverse magnetic field fluctuations, $|\mathrm{FFT}(\delta B_z/B_0)|^2$, obtained from the simulation at $\Omega_e t = 32.77$, in logarithmic scale. Upper and lower panels correspond to Case I and Case II, respectively.

show (in logarithmic scale) spatial power spectra of the transverse magnetic field fluctuations, $|\mathrm{FFT}\,(\delta B_z/B_0)|^2$ obtained from PIC simulations. These simulations confirm the existence of BEFHI and show a very good agreement with predictions from linear theory: fluctuations of higher intensity (top-right panel) are obtained in Case I, corresponding to the fastest mode of higher (maximum) growth rate (top-left panel).

Figure 6 shows temporal evolution of the magnetic energy density $W_B = \int \delta B^2/B_0^2\, dxdy$ (solid black for Case I and dashed grey for Case II) and electric energy density $W_E = \int \delta E^2/B_0^2\, dxdy$ (solid red for Case I and dashed pink for Case II), for the entire simulation period. We observe that for both cases the magnetic power, W_B, is dominant, increasing exponentially and reaching maximum intensity around $\Omega_e t \approx 40.8$

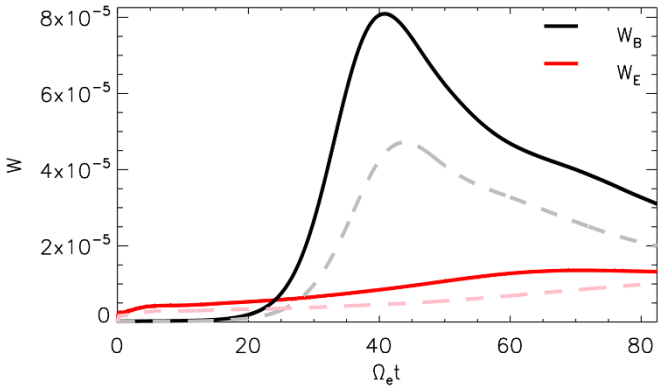

Figure 6. Temporal evolution of the magnetic and electric energy density for Case I ($v_d/c = 0.07$ and $\beta_e = 4.0$), and Case II ($v_d/c = 0.06$ and $\beta_e = 2.0$). Magnetic energy density is shown by black and grey lines, and electric energy density by red and pink, for cases I and II, respectively.

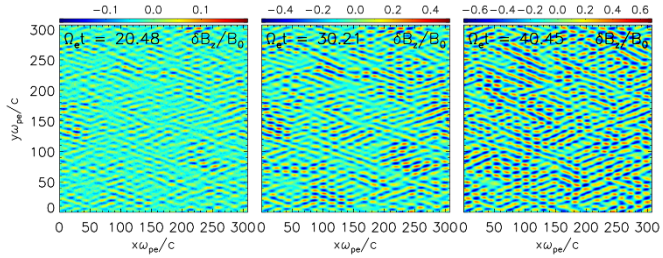

Figure 7. Snapshots of the transverse magnetic field fluctuations, $\delta B_z/B_0$, as a functions of normalized space, $x\omega_{pe}/c$ vs. $y\omega_{pe}/c$, for Case I. The snapshots are shown at: $\Omega_e t = 20.48$ (left), $\omega_e t = 30.21$ (middle), and $\Omega_e t = 40.45$.

for Case I (black) and $\Omega_e t \approx 43.8$ for Case II (grey). The onset time of the instability is earlier for Case I, and the maximum intensity reached is higher, as predicted by linear theory in figure 5. On the other hand, temporal variation of the electric energy density is very small in both cases providing a strong evidence that BEFHI is mainly of magnetic nature. It is worth noting that maximum values reached by the magnetic energy density are comparable with those obtained from the PIC simulations of AEFHI, see figure 3 in reference [4]. After the saturation of the instability, the magnetic energy density undergoes a gradual decrease due to the reabsorption of the wave energy, a feature commonly observed in the evolution of the electron firehose instability [4, 35]. The aperiodic nature of the BEFHI is clarified in figure 7, where we plot three snapshots of the transverse magnetic field fluctuations in the space domain $(\delta B_z(x,y)/B_0)$, for Case I (top panels in figure 5), at times at $\Omega_e t = 20.48$ (left), $\Omega_e t = 30.21$ (middle), and $\Omega_e t = 40.45$ (right). We observe that these fluctuations are mainly oblique to the background magnetic field and do not propagate in space, but only grow in time. This can be seen more clearly in the supplementary movie (stacks.iop.org/PPCF/62/075006/mmedia).

Figure 8 shows the reduced eVDF in parallel direction, $f(v_x)$, for different stages in the simulations of Case I (left) and

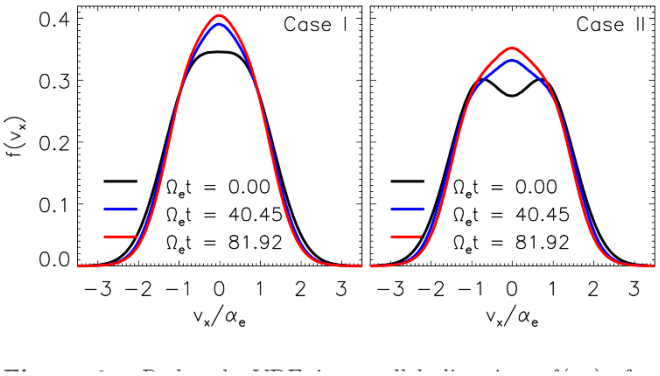

Figure 8. Reduced eVDF in parallel direction, $f(v_x)$, for different stages of the two cases, Case I (left) and Case II (right). In both cases the distribution are shown at: $\Omega_e t = 0$ (black), $\Omega_e t = 40.45$ (blue), and $\Omega_e t = 81.92$ (red).

Case II (right). For Case I, initially, at $\Omega_e t = 0$, it is not possible to distinguish the two peaks from each beam. However, due to the drift between both beams what we observe is like a flat-top distribution that then evolves to a more isotropic distribution, with a reduced drift, but with a significant accumulation of low-energy electrons resembling a Maxwellian core. The reduction in the drift velocity is more clearly shown in the right panel of figure 8, corresponding to Case II. Here it is clear that, as the BEFHI evolves in time, the initial gap between the two beams is filled, and the core of the combined distribution increases in a similar way as in Case I. Finally, it is worth to mention that our results from simulations show very little evolution in proton temperatures, parallel and perpendicular, and also, the proton distribution remains isotropic during the entire simulation period. For high drifts or/and low betas the BEFHI is indeed a fast growing mode (with maximum growth rates reaching an appreciable fraction of the electron gyrofrequency), and heavier protons do not have time to react.

2.3. Competition with electrostatic two-stream instability

With increasing the drift velocity BEFHI is competed by the electrostatic two-stream instability (ETSI), which develops (also aperiodically) with a maximum growth rate in parallel direction and becomes dominant mode for $v_d/\alpha_e > 1$. To explore this regime we chose Case III, with a higher drift $v_d/\alpha_e = 1.2$, and when the BEFHI is highly competed by the ETSI. Left panel in figure 9 shows the growth rate for this case, as a function of ck/ω_{pe} and θ, outlining the high growth rates of ETSI, with a maximum $\gamma_{\max}/\Omega_e \approx 1.91$ obtained at $ck/\omega_{pe} \approx 6.5$ in parallel direction $\theta = 0^\circ$. Some weak signatures of BEFHI are visible at high angles and low wavenumbers, where the growth rate reaches $\gamma_{\max}/\Omega_e \approx 0.31$, which is still higher than those obtained in Cases I and II, but much lower than that of ETSI. Right panel of figure 9 shows the same growth rates but in the $[k_x, k_y]$ plane, enabling to compare with the results from simulations. We ran a simulation for this case, using the same configuration described before, except that we have refined the grid to $\Delta x = \Delta y = 0.1\, c/\omega_{pe}$,

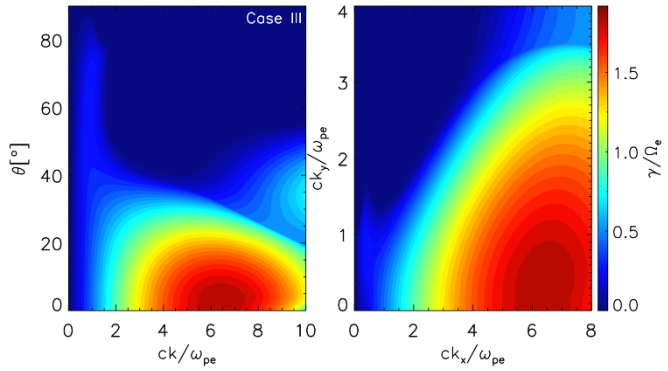

Figure 9. Case III ($\beta_e = 1$, $v_d/c = 0.06$): two equivalent dispersion plots of growth rates γ/Ω_e as functions of $[ck/\omega_{pe}, \theta]$ (left) and $[ck_x/\omega_{pe}, ck_y/\omega_{pe}]$ (right). Growth rates are dominated by ETSI (at large wave numbers) while the very low growth rates of BEFHI are barely visible at low wave numbers.

such that, we can resolve small scale fluctuations, appearing at large wavenumbers.

Figure 10 displays the power spectra from the simulations of Case III, parallel electric field fluctuations $|\mathrm{FFT}(\delta E_x/B_0)|^2$ (top) and transverse magnetic field fluctuations, $|\mathrm{FFT}(\delta B_z/B_0)|^2$ (bottom). Earlier at $\Omega_e t = 2.05$ (left panels) the ETSI and BEFHI coexist. The electric field power (top left) shows the presence of ETSI quasi-parallel modes around $ck/\omega_{pe} \approx 6$, in agreement with linear theory, e.g. in figure 9 right panel. At the same time, transverse magnetic field fluctuations (bottom left) show a very weak presence of the BEFHI modes at highly oblique angles around $ck_y/\omega_{pe} \approx 1$, again consistent with the results in figure 9.

For Case III the time evolutions of the magnetic (black) and electric (red) energy densities during simulation are shown in figure 11. Early in time ETSI is dominant (in agreement with linear theory), the electric energy grows faster but saturates ($\Omega_e t \approx 2.83$) at low levels, while the magnetic energy density starts to develop later but saturates ($\Omega_e t \approx 27.9$) at a much higher level, almost one order of magnitude higher than that of electric field. These results may correspond to a secondary magnetic instability, of the same nature as BEFHI, if the counter-beaming configuration is still present, or a mixture of AEFHI and BEFHI if the distribution is more relaxed. Snapshots corresponding to $\Omega_e t = 18.94$ in the right panels of figure 10 confirm that spectral power is concentrated in the transverse magnetic field at highly oblique angles (around $ck_x/\omega_{pe} \approx 0.3$ and $ck_y/\omega_{pe} \approx 0.8$).

The fast inhibition of the ETSI and the later dominance of (electro-)magnetic instability can be explained by looking at the time evolution of the velocity eVDF and its moments, which are described in figures 12 and 13. Figure 12 shows four instants from the evolution of the reduced eVDF along the magnetic field direction. The initial configuration (black) corresponds to two clearly separated beams unstable to the ETSI. As the simulation evolves the gap between each peak is filled, which means that the drift velocity is decreasing, or/and thermal spread of each beam is increasing. These effects lead to the saturation of ETSI. By the time the ETSI has saturated

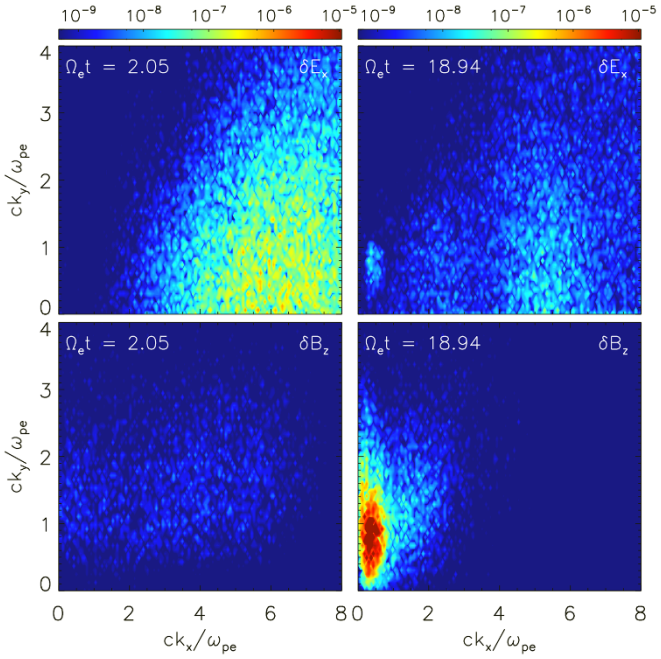

Figure 10. Power spectra of the parallel electric and transverse magnetic field fluctuations, $|\mathrm{FFT}(\delta E_x/B_0)|^2$ (top) and $|\mathrm{FFT}(\delta B_z/B_0)|^2$ (bottom), respectively, obtained for different stages of the simulation for Case III. Left panels show $\Omega_e t = 2.05$ and right panels $\Omega_e t = 18.94$..

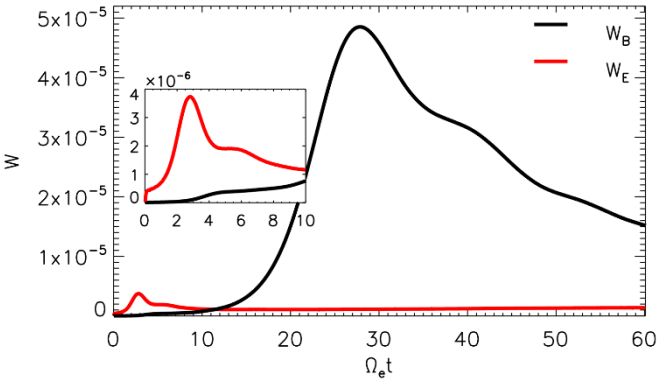

Figure 11. Temporal evolution of the magnetic and electric energy density for Case III.

($\Omega_e t = 2.83$) it is still possible to distinguish each beam, and drift velocity is still significant (red line), so the distribution is still unstable. However, at this stage the drift between the beams is already smaller than the thermal speed, such that we can expect BEFHI to become dominant. As the simulation and the BEFHI evolve, the counter-beaming distriution is further relaxed by completely filling the gap and forming a plateau in parallel direction. This is the moment ($\Omega_e t = 27.9$, blue curve in figure 12) when the BEFHI magnetic field starts to saturate. The relaxation of the counter-beaming distribution (isotropisation, thermalization) continues after the instability saturation, apparently as an effect of secondary instabilities, e.g. BEFHI combined with AEFHI. This prospect is also supported by a

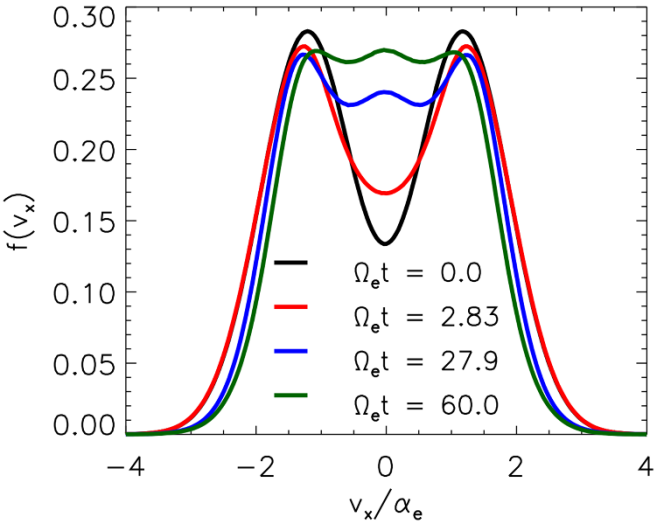

Figure 12. Reduced eVDF in parallel direction, $f(v_x)$, for different stages of Case III.

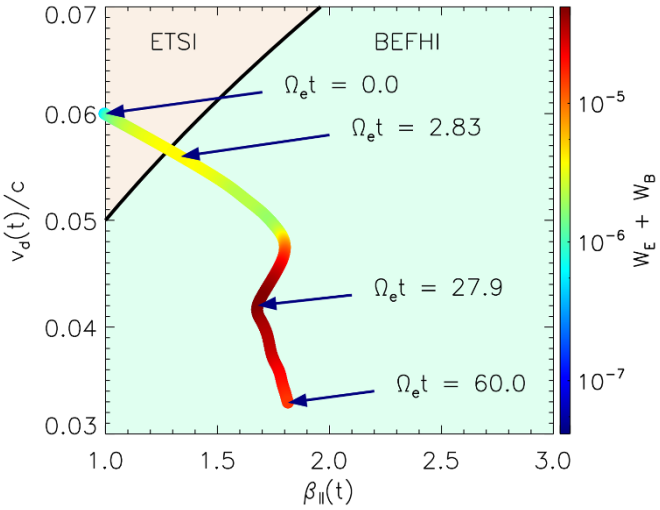

Figure 13. Dynamical path of the simulation for Case III, $v_d(t)/c$ vs. $\beta_{\parallel}(t)$. Color palette indicates the total electromagnetic energy density in logarithm scale. Black line shows the condition $v_d = \alpha_e$, as in figure 3.

slow decrease in time of the magnetic energy density after saturation (figure 11). At the end of our simulation ($\Omega_e t = 60.0$) the distribution in figure 12 shows a plateau in parallel direction (with some evidences of a small core formation at low energies), and because in perpendicular direction the distribution did not change much, we can talk about an effective temperature anisotropy $T_{\parallel} > T_{\perp}$ most unstable to the AEFHI.

Explanations can be added from the temporal evolution of macroscopic parameters in figure 13, where we follow dynamical paths in terms of v_d, $\beta_{\parallel}$, and total EM energy density. Initially the counter-beams are destabilized by the ETSI, which dominates and determines the initial evolution. We observe that the simulation evolves towards the regime dominated by the BEFHI, by reducing the drift and increasing the parallel plasma beta. By the time $\Omega_e t = 2.83$ the simulation has crossed the threshold $v_d = \alpha_e$, to a regime where BEFHI starts to develop and dominate, that is followed by a reduction of the electric field energy density. After the saturation of ETSI the electromagnetic energy density grows again, but this time because of an increase of the magnetic energy density induced by the BEFHI. Until its saturation at $\Omega_e t = 27.9$, the instability grows at the expense of both the drift between the beams and plasma beta. Then, the magnetic energy density decreases (see figure 11), but the fluctuations still act contributing to the relaxation of the distribution by diffusion in velocity space. The drift is further reduced, but parallel plasma beta is slightly increased, confirming an effective thermalization and heating of electrons in parallel direction.

3. Conclusions

In the present paper we have used linear theory and PIC simulations to show that in a magnetized plasma, the field-aligned counter-beaming populations of electrons can excite an aperiodic oblique instability. We have called this the beaming electron firehose instability (BEFHI), due to many similarities with the aperiodic electron firehose instability (AEFHI) driven by anisotropic temperatures $T_{\parallel} > T_{\perp}$. It is worth mentioning that the aperiodic nature of this instability is a direct consequence of the perfectly symmetric initial configuration. Breaking the symmetry by changing relative densities or/and temperatures of the beams will alter many properties of this instability. For symmetric counter-beaming populations of electrons, i.e. with the same densities, temperatures and beaming speeds, we can also associate an effective temperature anisotropy, but taking it with precaution, only for less energetic beams and not preventing a competition of BEFHI with electrostatic instabilities. Growth rates are highly sensitive to the variation of plasma parameters, increasing with the drift (beaming) speed (for a fixed plasma beta), and lowering with the increase of plasma beta (for a fixed beaming speed). In figure 3 we have provided the instability thresholds as contours of maximum growth rates, in terms of drifting speed and the electron plasma beta. Theory also predicts that this instability may coexist and interplay with the electrostatic two-stream instability (ETSI), that may develop when beaming speed (v_d) exceeds the thermal speed (α). However, the BEFHI remains dominant as long as the beaming speed is less than thermal speed. For more energetic beams with $v_d > \alpha_e$ the ETSI develops faster, with maximum growth rates almost one order of magnitude higher than those obtained for BEFHI.

We have confirmed the existence of the aperiodic BEFHI described in the linear theory, through PIC simulations. First, we have shown that for low drifts ($v_d < \alpha_e$) the BEFHI generates purely growing magnetic field fluctuations, oscillating in space obliquely to the background magnetic field, in agreement with predictions from linear theory. The magnetic field grows at the expense of the relative drift between the beams, and counter-beaming distribution become more isotropic, resembling a non-drifting Maxwellian by the end of the simulation. Similar to the AEFHI, the simulations show the same feedback between waves and particles, with the

electromagnetic energy density saturating and then decreasing while the electrons are heated in parallel direction [4, 35].

Using PIC simulations we have also investigated an extended existence of BEFHI for higher drifts $v_d > \alpha_e$, when the ETSI develops first. The counter-beaming distribution changes significantly under the influence of electrostatic fluctuations, by reducing the drift and increasing plasma beta, which both inhibit the ETSI. However, this relaxation of counter-beaming electrons lead to conditions favorable to BEHFI, e.g. whenever $v_d < \alpha_e$, it starts developing. In this case the BEFHI develops as a secondary instability but it reaches the same levels of electromagnetic energy density (much higher than the primary electrostatic fluctuations). It contributes to a further relaxation of counter-beaming electrons (as already described for $v_d < \alpha_e$), that in turn determines the saturation of the instability.

We expect our present results to be relevant in many specific applications of plasma beams, e.g. in astrophysical and fusion scenarios, helping us to understand their time evolution and stability, especially at the short timescales when beams are still accelerated and their beaming speed is lower than the local thermal speed. Future studies should consider more general situations of asymmetric beams, when the density or temperature contrasts may significantly change the properties of BEFHI.

Acknowledgments

These results were obtained in the framework of the projects SCHL 201/35-1 (DFG-German Research Foundation), C14/19/089 (C1 project Internal Funds KU Leuven), G0A2316N (FWO-Vlaanderen), and C 90347 (ESA Prodex 9). S M Shaaban acknowledges support by a FWO Postdoctoral Fellowship, grant No. 12Z6218N. P S Moya is grateful for the support of KU Leuven BOF Network Fellowship NF/19/001, and ANID Chile through FONDECyT Grant No. 1191351. The computational resources and services used in this work were provided by the VSC (Flemish Supercomputer Center), funded by the Research Foundation Flanders (FWO) and the Flemish Government department EWI.

ORCID iDs

R A López https://orcid.org/0000-0003-3223-1498
M Lazar https://orcid.org/0000-0002-8508-5466
S M Shaaban https://orcid.org/0000-0003-0465-598X
S Poedts https://orcid.org/0000-0002-1743-065
P S Moya https://orcid.org/0000-0002-9161-0888

References

[1] Camporeale E and Burgess D 2008 *J. Geophys. Res. Sp. Phys.* **113** A07107
[2] Remya B, Reddy R V, Tsurutani B T, Lakhina G S and Echer E 2013 *J. Geophys. Res. Sp. Phys.* **118** 785–93
[3] Hellinger P and Štverák Š 2018 *J. Plasma Phys.* **84** 905840402
[4] López R A, Lazar M, Shaaban S M, Poedts S, Yoon P H, Viñas A F and Moya P S 2019 *Astrophys. J. Lett.* **873** L20
[5] Palodhi L, Califano F, Dieckmann M E and Pegoraro F 2019 *Pramana* **93** 87
[6] Weibel E S 1959 *Phys. Rev. Lett.* **2** 83–4
[7] Fried B D 1959 *Phys. Fluids* **2** 337
[8] Schlickeiser R 2005 *Plasma Phys. Control. Fusion* **47** A205–A218
[9] Lazar M, Schlickeiser R, Wielebinski R and Poedts S 2009 *Astrophys.* J. **693** 1133–41
[10] Stockem A, Dieckmann M E and Schlickeiser R 2008 *Plasma Phys. Control. Fusion* **50** 025002
[11] Bret A 2009 *Astrophys.* J. **699** 990–1003
[12] Noreen N, Yoon P H, López R A and Zaheer S 2017 *J. Geophys. Res. Sp. Phys.* **122** 6978–90
[13] Shaaban S M, Lazar M, Astfalk P and Poedts S 2018 *J. Geophys. Res. Sp. Phys.* **123** 1754–1766
[14] Li X and Habbal S R 2000 *J. Geophys. Res. Sp. Phys.* **105** 27377–85
[15] Shaaban S M, Lazar M, López R A, Fichtner H and Poedts S 2019 *Mon. Not. R. Astron. Soc.* **483** 5642–8
[16] Štverák Š, Trávníček P, Maksimovic M, Marsch E, Fazakerley A N and Scime E E 2008 *J. Geophys. Res. Sp. Phys.* **113** A03103
[17] Bale S D, Kasper J C, Howes G G, Quataert E, Salem C and Sundkvist D 2009 *Phys. Rev. Lett.* **103** 211101
[18] Fox W, Fiksel G, Bhattacharjee A, Chang P Y, Germaschewski K, Hu S X and Nilson P M 2013 *Phys. Rev. Lett.* **111** 225002
[19] Che H, Goldstein M L and Viñas A F 2014 *Phys. Rev. Lett.* **112** 061101
[20] Zhang W S, Cai H B and Zhu S P 2018 *Plasma Phys. Control. Fusion* **60** 055001
[21] Du B, Cai H B, Zhang W S, Tian J M, Zhang E H, Zou S Y, Chen J and Zhu S P 2019 *Plasma Phys. Control. Fusion* **62** 025017
[22] Vocks C, Salem C, Lin R P and Mann G 2005 *Astrophys.* J. **627** 540–9
[23] Umeda T, Omura Y, Miyake T, Matsumoto H and Ashour-Abdalla M 2006 *J. Geophys. Res.* **111** A10206
[24] Che H, Goldstein M L, Salem C S and Viñas A F 2019 *Astrophys.* J. **883** 151
[25] Lapenta G, Markidis S, Marocchino A and Kaniadakis G 2007 *Astrophys.* J. **666** 949–54
[26] Marsch E 2006 *Living Rev. Sol. Phys.* **3** 1–100
[27] Tautz R C 2011 *Phys. Plasmas* **18** 012101
[28] Skoutnev V, Hakim A, Juno J and TenBarge J M 2019 *Astrophys. J. Lett.* **872** L28
[29] Shaaban S M, Lazar M and Poedts S 2018 *Mon. Not. R. Astron. Soc.* **480** 310–19
[30] López R A, Shaaban S M, Lazar M, Poedts S, Yoon P H, Micera A and Lapenta G 2019 *Astrophys. J. Lett.* **882** L8
[31] Tong Y, Vasko I Y, Pulupa M, Mozer F S, Bale S D, Artemyev A V and Krasnoselskikh V 2019 *Astrophys. J. Lett.* **870** L6
[32] Tong Y, Vasko I Y, Artemyev A V, Bale S D and Mozer F S 2019 *Astrophys.* J. **878** 41
[33] López R A, Viñas A F, Araneda J A and Yoon P H 2017 *Astrophys.* J. **845** 60
[34] Matsumoto H and Omura Y (eds) 1993 *Computer Space Plasma Physics: Simulation Techniques and Software* (Tokyo: Terra Scientific)
[35] Yoon P H, López R A, Seough J and Sarfraz M 2017 *Phys. Plasmas* **24** 112104